ICARUS 84, 334–351 (1990)

The Shape of Eros

S. J. OSTRO, K. D. ROSEMA, AND R. F. JURGENS

Jet Propulsion Laboratory, California Institute of Technology, Pasadena, California 91109

Received June 26, 1989; revised September 6, 1989

The convex hull of Eros' polar silhouette, estimated from radar echo spectra obtained in 1975 by R. F. Jurgens and R. M. Goldstein (1976, *Icarus* 28, 1–15), provides new information about this asteroid's shape. Monte Carlo simulations are used to optimize the estimation, to explore the nature and severity of associated errors, and to guide bias-correction procedures. Eros' hull is shaped like a rounded trapezoid, whose long and short bases faced Earth during epochs of primary and secondary maxima, respectively, in the January 1975 optical lightcurves. The nonaxisymmetric shape helps to explain odd harmonics in Eros' echo spectral signature as a function of rotation phase, whose presence cannot be accounted for by homogeneous ellipsoid models. The extreme breadths of Eros' polar silhouette are within a few kilometers of 35 and 16 km. Additional constraints on Eros' figure are obtained by inverting an optical lightcurve to estimate the asteroid's "mean cross section," which is a two-dimensional average of the three-dimensional shape. Eros' mean cross section and polar silhouette have similar elongations. The hull estimate permits previously reported radar time-delay and Doppler-frequency measurements to be referenced directly to Eros' center of mass.

I. INTRODUCTION

433 Eros, discovered by G. Witt in 1898, is distinguished by being the first known Mars-crosser, the first asteroid to show a lightcurve (von Oppolzer 1901), and the first asteroid to be observed while occulting a star (O'Leary *et al.* 1976). The discovery of Eros' large orbital eccentricity attracted considerable interest and catalyzed a series of dynamical studies, including Russell's (1900) doctoral dissertation. Triangulation of the distance to Eros and analyses of perturbations on Eros' orbit provided the most reliable values for the solar parallax and the AU (i.e., for the scale of the solar system expressed in terrestrial units) until the advent of planetary radar ranging in the early 1960s (McGuire *et al.* 1961).

Eros made its closest approach to Earth in this century (0.15 AU) on January 13, 1975, and was favorably placed for telescopic investigation within several months of that date. A campaign was organized to seize this opportunity using available astronomical techniques, and the May 1976 issue of *Icarus* was devoted to papers reporting the observations. Zellner (1976) noted that no other solar system body in its size range had been so thoroughly observed, and summarized the results as follows:

> Newly available photometric, polarimetic, spectroscopic, thermal-radiometric, radar, and occultation results are synthesized in order to derive a coherent model for Eros. The geometric albedo is 0.19 ± 0.01 at the visual wavelength, and the overall dimensions are approximately $13 \times 15 \times 36$ km. The rotation is about the short axis, in the direct sense, with a sidereal period of $5^h16^m\ 13.4^s$. The pole of rotation lies within a few degrees of ecliptic coordinates $\lambda = 16°$ and $\beta = +11°$. Eros is uniformly coated with a particulate surface layer several millimeters thick. It has an iron-bearing silicate composition, similar to that of a minority of main-belt asteroids, and probably identifiable with H-type ordinary chondrites.

The constraints on Eros' shape, derived primarily from optical lightcurves (e.g., Dunlap 1976, Millis *et al.* 1976, Scaltriti and Zappalà 1976) and 3.5-cm radar observations (Jurgens and Goldstein 1976), were

0019-1035/90 $3.00

obtained within the framework of some assumed, axisymmetric model. Such approaches were appropriate first approximations, but their inadequacy was apparent from the presence of odd harmonics in the lightcurves and in the rotation-phase dependence of the radar signatures. In analyzing the latter, Jurgens and Goldstein (1976) used a homogeneous, triaxial ellipsoid model (Jurgens 1982), but they warned of that model's inability to accommodate a strong, predominantly first-harmonic wobble in the echo spectral shape. The presence of the fundamental Fourier component indicated that Eros' figure and/or it's radar scattering properties are not axisymmetric, but it was not at all clear how one might obtain information about the nature of the asymmetry.

Recently, Ostro *et al.* (1988a) introduced a theoretical approach to asteroid echo-spectral analysis that follows naturally from the geometric relation between spectral edge frequencies and the shape of a rotating asteroid. This approach uses the *extent* of the spectra to determine the convex envelope, or hull, of the asteroid's polar silhouette—a pole-on projection of the asteroid with concavities "filled in." Ostro *et al.* (1988a) showed how to estimate the hull, developed error-analysis techniques, and studied the relation between the accuracy of a hull estimate and the parent data set's signal-to-noise ratio.

Here we estimate Eros' hull and use the results to evaluate, and in a few instances refine, the 1976 constraints on the asteroid's physical properties. In the next section, we describe the Eros radar data set used in our calculations. In Section III, we briefly review important geometric relations and hull estimation mathematics, and then describe in considerable detail the logic and procedures underlying optimization of our hull estimator. Practical aspects of hull estimation not confronted by Ostro *et al.* (1988a) are addressed here. For example, for a given set of echo spectra, the accuracy of a hull estimate turns out to depend on the data set's frequency resolution and rotation-phase resolution. The Eros data are "overresolved" in each domain, forcing us to smooth the data and to search for the best phase/frequency filter. In Section IV, we present our estimate of Eros' hull and then, armed with new information about the asteroid's shape, revisit several intriguing characteristics of the optical and radar data.

II. THE EROS RADAR DATA

We worked with 199 echo spectra from Goldstone X-band (8495-MHz, 3.53-cm) observations conducted on January 19, 24, 25, and 26, 1975 (Table I of Jurgens and Goldstein 1976). On these dates, reception was in the sense of *circular* polarization *orthogonal* to that transmitted. These "OC" echoes, which contain most of the power in back-reflections from smooth components of Eros's surface, are approximately three times stronger than the SC (same circular) echoes.

The raw frequency resolution was 1.95 Hz on January 19 and 2.73 Hz on the last three dates; we interpolated between spectral estimates from the January 19 data to find values at 2.73-Hz intervals. Eros' echo bandwidth was known to range from ~300 to ~700 Hz, so the fractional spectral resolution was ~0.01. The echoes lie near the middle of a spectral window ~1200 Hz wide.

The integration time per spectrum was ~150 sec, during which Eros rotated through 2.8° of rotation phase. The rotation-phase coverage of the 199 spectra is very thorough and fairly uniform, with no gaps larger than 6°.

The spectral elements have units of standard deviations of the receiver noise, and each spectrum is tagged with γ, the value of the standard deviation in units of square kilometers of radar cross section per 2.73-Hz resolution cell. γ is constant for any given spectrum, but varies between spectra because of run-to-run variations in radar system sensitivity and target distance.

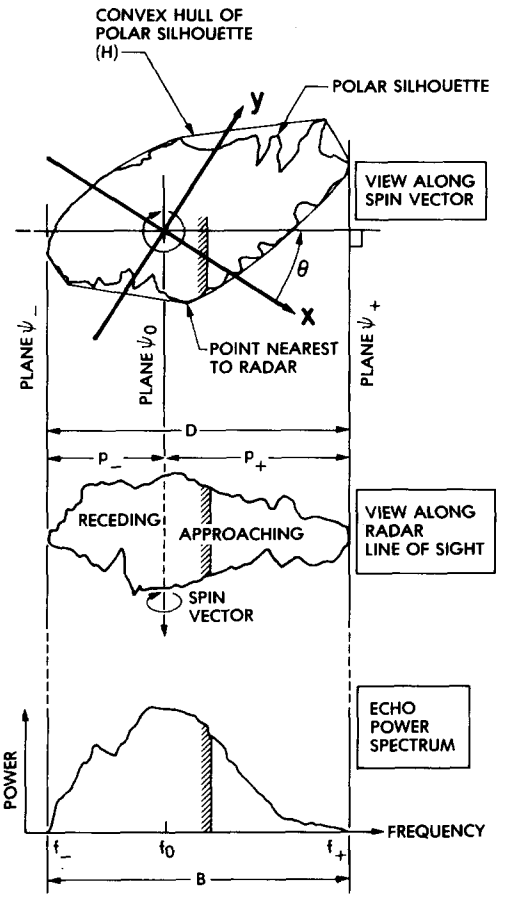

FIG. 1. Geometric relationships between an asteroid's shape and its echo power spectrum. The plane ψ_0 contains the line of sight and the asteroid's spin vector. Echo from any portion of the asteroid intersecting ψ_0 has Doppler frequency f_0. The cross-hatched strip of power in the spectrum corresponds to echoes from the cross-hatched strip on the asteroid. The x, y coordinate system (dark lines) rotates with the asteroid. Reproduced, with permission, from Ostro *et al.* (1988a).

III. THEORY AND PRACTICE OF HULL ESTIMATION

A. Geometric Relations and Definitions

Figure 1 sketches the relation between an asteroid's hull and an echo power spectrum obtained at rotation phase θ. One can think of the hull, $\underline{H}$, as the shape of a rubber band stretched around the projection of the asteroid onto its equational plane.

An asteroid's instantaneous echo power spectrum has a bandwidth given by

$$B = (4\pi D/\lambda P) \cos \delta, \qquad (1)$$

where P is the apparent spin period, δ is asteroid-centered declination of the radar, and D is the sum of the "support distances" p_+ and p_- *from* the plane ψ_0 containing the asteroid's apparent spin vector Ω and the line of sight *to* the surface elements with the greatest positive (approaching) and negative (receding) radial velocities. In the figure, the planes ψ_+ and ψ_- are parallel to ψ_0 and tangent to the asteroid's approaching and receding limbs; ψ_+ and ψ_- are at distances p_+ and p_- from ψ_0; f_0, f_+, and f_- are the Doppler frequencies of echoes from portions of the asteroid intersecting ψ_0, ψ_+, and ψ_-; and $B = f_+ - f_- = 4\pi(p_+ + p_-)(\lambda P)^{-1} \cos \delta$.

The "support function," $p(\theta) \equiv p_+(\theta) \equiv p_-(\theta + 180°)$, is a periodic function of rotation phase θ. Santaló (1976) shows that

$$p(\theta) + p''(\theta) = r(\theta), \qquad (2)$$

where the primes denote differentiation with respect to θ, and $r(\theta)$ is the radius of curvature of $\underline{H}$ where ψ_+ touches $\underline{H}$. The Cartesian coordinates of $\underline{H}$ are given by

$$\begin{aligned} x(\theta) &= p(\theta) \cos \theta - p'(\theta) \sin \theta \\ y(\theta) &= p(\theta) \sin \theta + p'(\theta) \cos \theta, \end{aligned} \qquad (3)$$

where the x, y coordinate system (dark lines in the figure) rotates with the asteroid.

B. Mathematics of Hull Estimation

Henceforth, we assume prior knowledge of the asteroid's apparent rotation period. For the moment, let us also assume that we know the Doppler frequency f_0 corresponding to echoes from the center of mass.

Estimation of $\underline{H}$ can be thought of as a three-step process:

Step 1. Generate a data vector of support function estimates from the spectra. We derive two numbers, $p(\theta)$ and $p(\theta + 180°)$, from a spectrum acquired at rotation phase θ, so L spectra yield a $2L$-element data vector. *Note*: In this section, we use hertz as the

units for the support function and the hull, postponing until Section IV the conversion to kilometers, which requires a value of δ.

Step 2. Use least squares to fit an M-harmonic Fourier series to the data vector. That series has the form

$$p(\theta) = \sum_{n=0}^{M} a_n \cos n\theta + b_n \sin n\theta. \quad (4)$$

Let boldface denote matrices and T denote transpose. We define the data vector of support-function estimates

$$\mathbf{p}^{\mathrm{T}} = (p_1, p_2, \ldots, p_{2L}) \quad (5)$$

and the vector of Fourier coefficients

$$\mathbf{x}^{\mathrm{T}} = (x_1, x_2, \ldots, x_{2M+1}) = (a_0, a_1, b_1, a_2, b_2, \ldots, a_M, b_M). \quad (6)$$

If the errors ε in the support-function estimates $\mathbf{p}$ are random variables with zero mean and covariance matrix $\mathbf{M} = \langle \varepsilon\varepsilon^{\mathrm{T}} \rangle$, then the weighted-least-squares estimate of $\mathbf{x}$ is $\hat{\mathbf{x}} = \mathbf{B}^{-1}\mathbf{A}^{\mathrm{T}}\mathbf{M}^{-1}\mathbf{p}$, where $\mathbf{B} = \mathbf{A}^{\mathrm{T}}\mathbf{M}^{-1}\mathbf{A}$ and the i^{th} row of $\mathbf{A}$ is $(1, \cos\theta_i, \sin\theta_i, \cos 2\theta_i, \sin 2\theta_i, \ldots, \cos L\theta_i, \sin L\theta_i)$. The weighted sum of squared residuals, $Q(\mathbf{x}) = (\mathbf{p} - \mathbf{A}\mathbf{x})^{\mathrm{T}}\mathbf{M}(\mathbf{p} - \mathbf{A}\mathbf{x})$, defines a quadratic hypersurface with minimum $Q(\hat{\mathbf{x}})$. The covariance matrix for errors in the parameter estimates is $\mathbf{V} = \mathbf{B}^{-1}$ and the Fourier model for the data is $\hat{\mathbf{p}} = \mathbf{A}\hat{\mathbf{x}}$.

Since $\underline{\mathrm{H}}$ is convex, its radius-of-curvature function is nonnegative:

$$r(\theta) = p(\theta) + p''(\theta) \geq 0. \quad (7)$$

In practice, our estimate of $\underline{\mathrm{H}}$ will be an N-sided convex polygon corresponding to a model support function that satisfies

$$r(2\pi k/N) = r(\theta_k) = p(\theta_k) + p''(\theta_k) \geq 0, \quad k = 1, \ldots, N. \quad (8)$$

These N inequality constraints would "automatically" be satisfied by $\hat{\mathbf{x}}$ if the spectra were continuous, contained no noise, and were available as a continuous vector function of rotation phase. In practice, echo spectra are discrete and noisy, and sample rotation phase imperfectly, so $\hat{\mathbf{x}}$ might not satisfy those constraints even though it minimizes the weighted sum of squared residuals $Q(\mathbf{x})$, and an additional step is required.

Step 3. Find the value $\hat{\hat{\mathbf{x}}}$ of $\mathbf{x}$ that minimizes $Q(\mathbf{x})$ subject to the N inequality constraints. $\hat{\hat{\mathbf{x}}}$ is the closest point to $\hat{\mathbf{x}}$ (in the $\mathbf{B}$ metric) that corresponds to a nonnegative radius-of-curvature function. Our task, to minimize the quadratic form $(\mathbf{x} - \hat{\mathbf{x}})^{\mathrm{T}}\mathbf{B}(\mathbf{x} - \hat{\mathbf{x}})$ subject to the constraints, is an example of the strictly convex quadratic programming problem. Ostro and Connelly (1984, Section IIC and Appendix B) describe this problem and its solution via a recursive projection method. For all the work described in this paper, we truncated Fourier series to $M = 10$ harmonics and applied the inequality constraints at $N = 96$ rotation phases.

C. Accuracy of Hull Estimation: Spectral-Frequency Resolution and Rotation-Phase Resolution

Whereas execution of steps 2 and 3 is straightforward, the best way of estimating the spectral edge frequencies (step 1) is not known. For simplicity, we use the closest zero crossings to f_0 as the values of $p(\theta)$ and $p(\theta + 180°)$ associated with a spectrum taken at rotation phase θ. Note that this or any other support-function estimator might introduce systematic uncertainty into the hull estimation. This uncertainty will not be known a priori because the true shape of the spectral edges is unknown, so it will be prudent to assess the severity of systematic errors by performing numerical simulations.

We expect our "zero-crossing estimator" to yield hulls whose accuracy depends on the frequency resolution, the rotation-phase sampling, and the signal-to-noise ratio of the parent spectra. For the Eros data, the "total" signal-to-noise ratio (SNR) of the optimally filtered, weighted sum of all the spectra is about 70 standard deviations. Given

the analysis of Ostro *et al.* (1988a), we knew that with an SNR that low, estimation of $\underline{H}$ from the raw spectra would be very inaccurate. That is, the spectra are so finely resolved that the echo edges are overwhelmed by noise, and application of the zero-crossing estimator would yield a hull with a size much smaller than the true one and presumably with a grossly incorrect shape.

To overcome the low SNR of the Eros spectra, we can either (i) smooth the spectra to a coarser frequency resolution, thereby improving their SNR, and/or (ii) form weighted averages of several spectra taken at similar rotation phases, i.e., increase the SNR by smoothing the spectra to a coarser rotation-phase resolution. Of course, we would like to do this "frequency and/or phase filtering" in a manner that optimizes the accuracy of the hull estimate. The following strategy was used to evaluate any given choice of frequency resolution and phase resolution:

i. Use Jurgens and Goldstein's (1976) triaxial ellipsoid model to generate 199 noise-free echo spectra having 2.73-Hz resolution and the same relative phases as the actual Eros spectra.

ii. Add Gaussian noise supplied by a random number generator to each of the model spectra, scaling the standard deviation of the noise to match that in the corresponding spectrum of the actual data.

iii. Smooth the noise-contaminated model spectra to a frequency resolution Δf and a phase resolution $\Delta\theta$ (Appendix).

iv. Estimate the model's hull according to the three-step procedure described earlier. Then compare the estimate, $\hat{H}(\Delta\theta, \Delta f)$, to the true hull (a known ellipse), and assess the accuracy provided by this choice of phase/frequency smoothing.

In (ii), note that the vector of noise constitutes a *single* realization of the parent random process. To better assess the variance of this estimator, we repeated the simulation for five independent noise realizations. This entire, five-realization simulation was done for each choice of phase/frequency smoothing.

D. Optimization with Respect to $\Delta\theta$ and Δf

Figure 2 shows results for all nine combinations of the values: $\Delta\theta = 15°$, 20°, and 25°, and $\Delta f = 25$, 30, and 35 Hz, covering the region yielding the most satisfactory results. The accuracy of $\hat{H}(\Delta\theta, \Delta f)$ deteriorates rapidly outside this region.

It is useful to define a simple measure of the "distance" Ω between two hulls $\underline{H}_1$ and $\underline{H}_2$ as the root-sum-square of the distances between those two polygon's corresponding vertices:

$$N\Omega^2 = \sum_{k=1}^{N} [(x_1 - x_2)^2 + (y_1 - y_2)^2]_k. \quad (9)$$

The figure gives the mean value and rms dispersions of the error distance between $\hat{H}(\Delta\theta, \Delta f)$ and the true (elliptical) hull for each of the nine, five-simulation sets. In each set, the five distances' mean value quantifies the estimator's bias. The square of the five distances' dispersion about their mean can be taken as a crude indicator of the estimator's variance.

The minimum-bias estimator in the figure is at $(\Delta\theta, \Delta f) = (20°, 30\text{ Hz})$, but the differences among the nine values of $(\Delta\theta, \Delta f)$ do not seem highly significant. Therefore, although we will refer to $\underline{E}(20°, 30\text{ Hz})$ as the optimum estimator, we will apply all nine estimators to the Eros data, and will use the spread in the results as a gauge of estimation error.

Our estimator recovers the true hull's maximum breadth quite accurately but overestimates the minimum breadth by ~20%. This *positive bias* in the estimated hull's minimum dimension probably is caused by a combination of the limited SNR and the fact that the minimum-bandwidth orientation is seen very briefly, despite the fairly uniform and thorough phase coverage provided by the Goldstone data. (Note that phase filter-

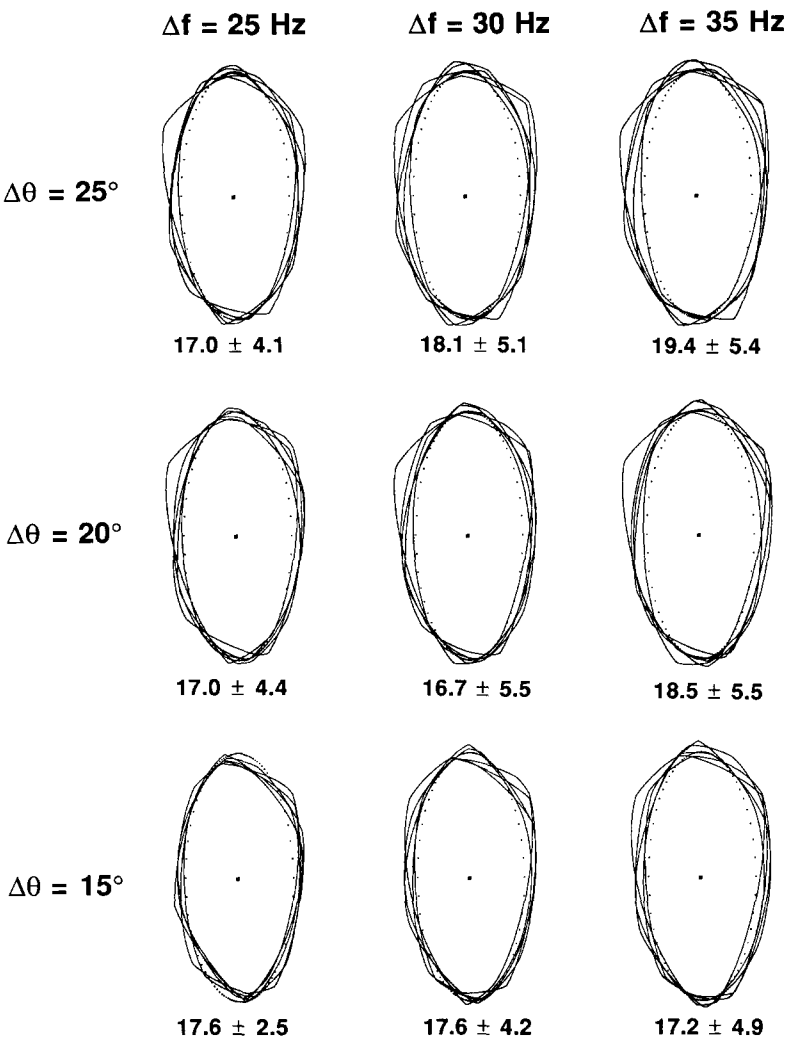

FIG. 2. Hull estimates for simulations designed to explore the dependence of estimation accuracy on the data's frequency resolution (Δf) and rotation-phase resolution ($\Delta\theta$). The dotted profile is the true hull of an ellipsoidal model asteroid and the solid curves are estimates derived from simulated echo spectra contaminated with noise. The five profiles at any given value of (Δf, $\Delta\theta$) correspond to five different realizations of the noise-generating random process. The difference between a hull estimate and the true ellipse is quantified by an error distance Ω defined in Eq. (9), and this figure gives the mean value and rms dispersion of Ω for each five-simulation set.

ing "works against" our seeing the minimum echo bandwidth, but would not keep us from seeing the maximum bandwidth.)

E. Center Frequency as a Free Parameter

So far, we have assumed prior knowledge of f_0, the Doppler frequency corresponding to echoes from Eros' center of mass. In reality, that frequency is a function of time, t. During the Eros radar observations, the receiver was continuously tuned to the echo using a prediction ephemeris that later proved to be accurate to within several tens of hertz (Fig. 2 of Jurgens

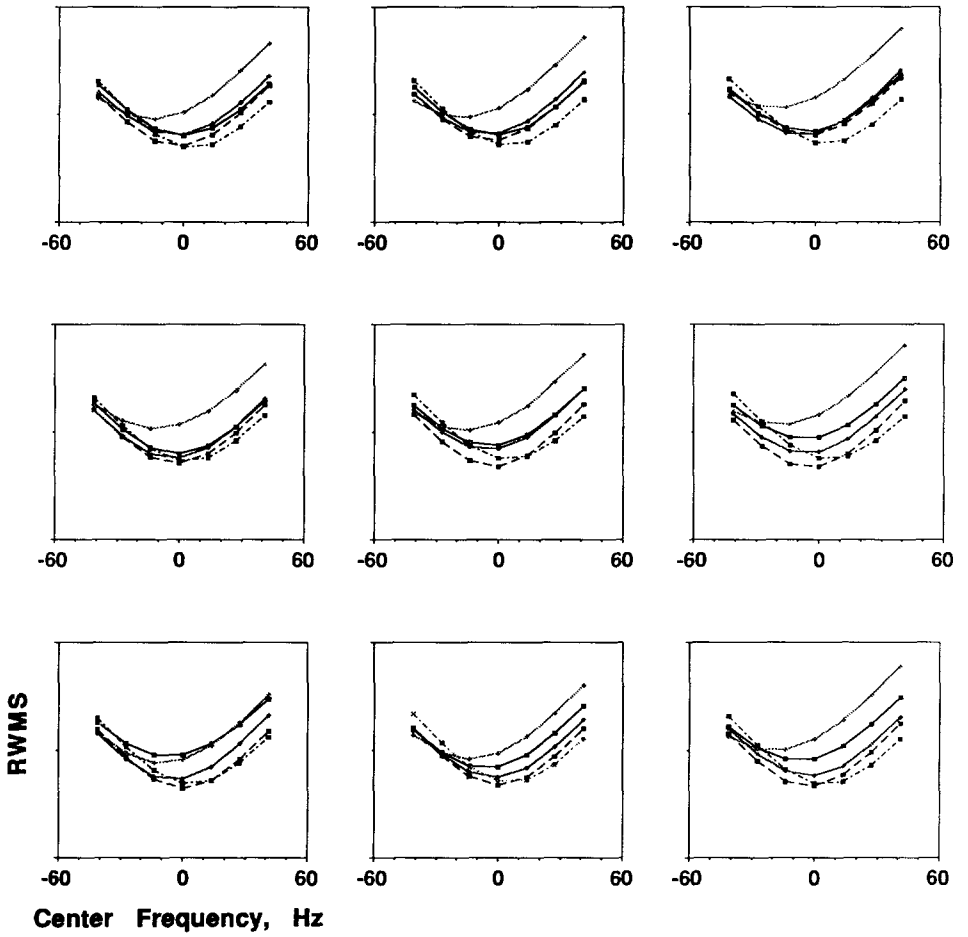

FIG. 3. Sensitivity of the hull estimators to center frequency for the model-ellipsoid simulations described in Section IIIE. The nine blocks of curves correspond to the nine drawings in Fig. 2. Within each block, the five curves correspond to five different noise realizations, as in Fig. 2. RWMS, defined in Eq. (10), is the root-weighted-mean-square residual between support-function data $\mathbf{p}$ and the support-function values $\hat{\mathbf{p}}$ corresponding to a hull estimate. Here, RWMS is plotted on arbitrary linear scales versus the center frequency f_0 used in the estimation, measured with respect to the true value.

and Goldstein 1976). The variation of the Doppler prediction error during the week of observations was expected to be much less than the data's frequency resolution (2.73 Hz).

Henceforth, let f_0 represent Eros' echo center frequency *relative* to the observing ephemeris. We wish to treat this offset as a free parameter, so we explored each estimator's sensitivity to f_0 by repeating *each* of the 45 simulations in Fig. 2 six more times, offsetting f_0 from its true value by ± 5, ± 10, and ± 15 frequency resolution cells. For each simulation, we calculated the root-weighted-mean-square postfit residual RWMS, defined by

$$\mathrm{RWMS}^2 = \left[\sum_{i=1}^{2L} (p_i - \hat{p}_i)^2 \, s_i^{-2}\right] \Big/ \left[\sum_{i=1}^{2L} s_i^{-2}\right], \quad (10)$$

and plotted the five-simulation-average RWMS versus offset frequency in Fig. 3.

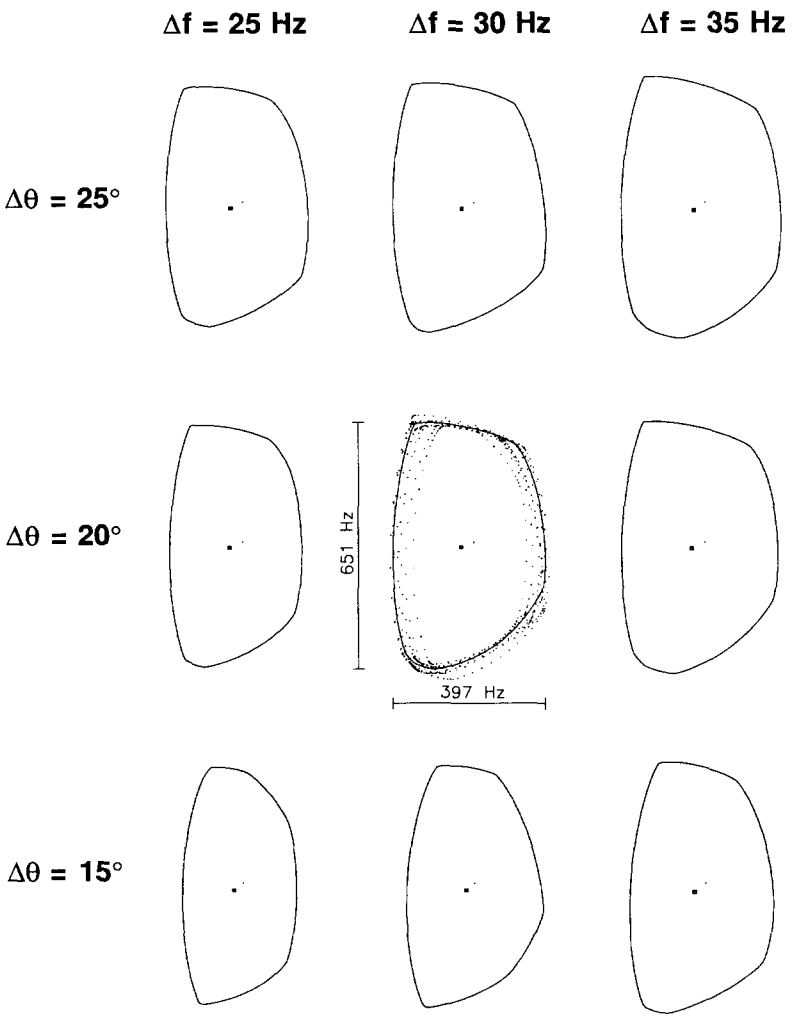

FIG. 4. "Raw" estimates of Eros' hull at nine values of phase/frequency resolution. The maximum and minimum breadths for the optimal estimate, $\hat{H}(20°, 30\ \text{Hz})$, are indicated. All profiles are plotted at the same scale. For each profile, the center of rotation is denoted by a tiny dot and the centroid is denoted by a large symbol. Dotted replicas of the eight profiles on the figure's periphery are superposed on $\hat{H}(20°, 30\ \text{Hz})$. The simulations described in Section IIID indicate that these estimations are biased, with the hull's minimum dimension being overestimated by ~20%. A bias-corrected version of the central drawing is shown in Fig. 6. See text.

On average, RWMS's minimum appears to be within ~10 Hz of the true value of f_0, although biases as large as ~20 Hz are evident in some of the individual curves.

IV. EROS' SHAPE

A. The Hull Estimate

Figure 4 shows results of applying each of the nine best estimators (Fig. 2) to the Eros data. The center drawing superposes $\hat{H}(20°, 30\ \text{Hz})$ and dotted replicas of the eight other estimates to permit more direct comparison of the profiles' sizes and shapes. Table I gives corresponding values of the hull's maximum and minimum widths, their ratio, and the distance of each estimate of Eros' hull from $\hat{H}(20°, 30\ \text{Hz})$. Table I also lists the goodness-of-fit statistic RWMS.

TABLE I

"RAW" EROS HULL ESTIMATES[a]

	Δf = 25 Hz	Δf = 30 Hz	Δf = 35 Hz
		Distance (Hz) from $\hat{H}$(20°, 30 Hz)	
$\Delta\theta$ = 25°	26.0	25.0	28.0
$\Delta\theta$ = 20°	37.3	0	12.5
$\Delta\theta$ = 15°	56.7	42.8	31.8
		Support-function RWMS (Hz)	
$\Delta\theta$ = 25°	42.8	45.5	51.6
$\Delta\theta$ = 20°	41.0	42.6	44.5
$\Delta\theta$ = 15°	48.5	51.1	48.0
		"Raw" maximum dimension (Hz)	
$\Delta\theta$ = 25°	638	663	702
$\Delta\theta$ = 20°	638	651	668
$\Delta\theta$ = 15°	630	647	666
		"Raw" minimum dimension (Hz)	
$\Delta\theta$ = 25°	368	397	414
$\Delta\theta$ = 20°	343	397	406
$\Delta\theta$ = 15°	296	356	373
		"Raw" Elongation	
$\Delta\theta$ = 25°	1.74	1.67	1.70
$\Delta\theta$ = 20°	1.86	1.64	1.65
$\Delta\theta$ = 15°	2.13	1.82	1.79

[a] Results for each of the nine estimators $\underline{E}(\Delta\theta, \Delta f)$, where $\Delta\theta$ and Δf are the rotation phase and spectral frequency resolutions. Table II shows results of applying bias corrections described in the text to the three lower 3 × 3 subtables.

The minimum in RWMS at $(\Delta\theta, \Delta f)$ = (20°, 25 Hz) is not a global minimum; another, nearly identical, local minimum occurs at $(\Delta\theta, \Delta f)$ = (20°, 15 Hz).

In Fig. 4, the Earth is toward the bottom of the page and the hull rotates clockwise about its center of mass (the small dot). We have rotated $\hat{H}$(20°, 30 Hz) to bring its minimum dimension normal to the line of sight with the longest side on the receding limb. *We define this orientation to have rotation phase* θ = 0°. Equivalent "minimum-breadth" orientations of the eight other estimates occur at rotation phases within 2.5° of 0°. This is excellent agreement in view of the 2.8° phase resolution of the individual spectra and the angular quantization (360°/N = 3.75°) used in our estimations. Consequently, we have rotated *all nine* hull estimates in Fig. 4 by the same amount.

Additional results associated with Eros' hull estimation are shown in Fig. 5 for the calculation of $\hat{H}$(20°, 30 Hz). The left box shows $\hat{\mathbf{p}}$ and $\hat{\mathbf{p}}$, and the right box shows the radius-of-curvature functions $\hat{\mathbf{r}}$ and $\hat{\mathbf{r}}$. The hull's bandwidth function,

$$\hat{B}(\theta) = \hat{p}(\theta) + \hat{p}(\theta + 180°), \quad (11)$$

is the uppermost curve in the top left plot; note that it contains only even harmonics. The corresponding "middle frequency function,"

$$\hat{f}_{\text{mid}}(\theta) = [\hat{p}(\theta) - \hat{p}(\theta + 180°)]/2, \quad (12)$$

is the lowest curve in that plot; note that it contains only odd harmonics.

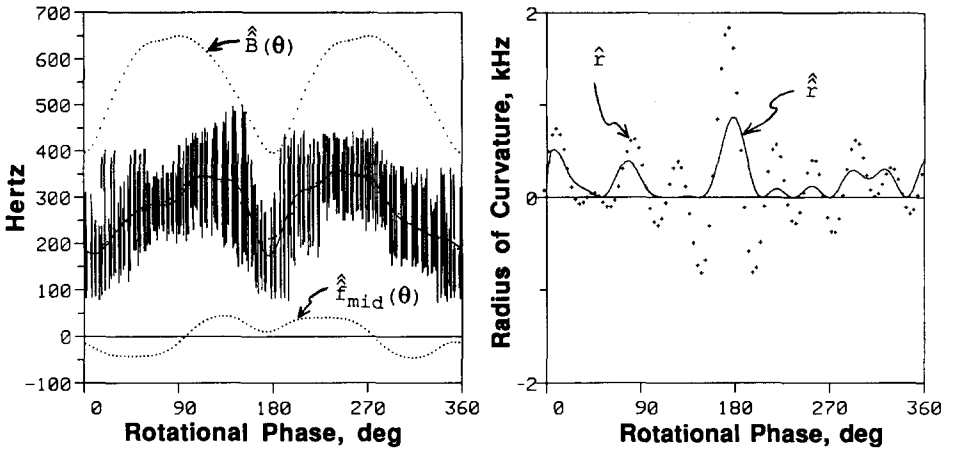

FIG. 5. Quantities associated with Eros' hull estimation, shown here for the calculation of $\hat{H}(20°, 30$ Hz), which is the solid profile in the center of Fig. 4. In the left-hand box, the vertical bars represent the support-function data p_i obtained from the echo spectra; each bar extends from $p_i - \varepsilon_i$ to $p_i + \varepsilon_i$, where the errors ε_i were determined a posteriori, as described in the Appendix. The solid curve through the support-function data is $\hat{\mathbf{p}}$, the unconstrained Fourier model. The dotted curve through the data is $\hat{\hat{\mathbf{p}}}$, the closest Fourier model to $\hat{\mathbf{p}}$ yielding a nonnegative radius-of-curvature function; $\hat{\hat{\mathbf{p}}}$ corresponds to the hull estimate via Eq. (3). The hull's bandwidth function $\hat{B}(\theta)$ and middle-frequency function $\hat{f}_{mid}(\theta)$ are defined by Eqs. (11) and (12). The radius-of-curvature functions $\hat{\mathbf{r}}$ and $\hat{\hat{\mathbf{r}}}$ in the right-hand figure are related to $\hat{\hat{\mathbf{p}}}$ and $\hat{\mathbf{p}}$ via Eq. (2).

The support function data are shown as vertical bars extending from $p_i - \varepsilon_i$ to $p_i + \varepsilon_i$, where the values of the errors ε_i were determined a posteriori, as described in the Appendix. Note that the fractional precision of *individual* support-function estimates is very low; the leverage in determining $\underline{\hat{H}}$ is furnished by the geometrical constraints in Eq. (7), i.e., by the fact that we are estimating a convex quantity.

How can we gauge the uncertainty in our estimate of Eros' hull? Recall from the discussion of the ellipsoid simulations that the systematic uncertainty in $\underline{E}(\Delta\theta, \Delta f)$ is quantified by the mean error distance Ω associated with any particular estimator, while the statistical uncertainty in $\underline{E}(\Delta\theta, \Delta f)$ is quantified by Ω's rms dispersion (Fig. 2). For $\underline{E}(20°, 30$ Hz), Ω's mean and rms values are 16.7 ± 5.5 Hz, so the systematic uncertainty is several times more severe than the statistical uncertainty. The sum of these two error components is 22.2 Hz, which is 72% as large as the average distance (31 Hz) of the solid profile $[\hat{\hat{H}}(\Delta\theta, \Delta f)]$ from the dotted profiles in Fig. 4 and 40% as large as the maximum distance (56.7 Hz) of the solid profile from a dotted profile. Thus, the "collective smear" of the profiles in the center drawing of Fig. 4 overstates the magnitude of the total error in our optimum estimator.

B. Bias Correction

As discussed earlier, the ellipsoid simulations yielded hull estimates whose longest dimension was estimated quite accurately but whose shortest dimension was overestimated by up to ~20%. Table II gives correction factors which, when multiplied by the five-realization-average values of the extreme breadths of the estimated hulls, result in the extreme breadths of the ellipsoid's actual, elliptical hull. For example, that ellipse has minimum and maximum breadths that are 82 and 100% of those of the five-realization-average value for the optimal estimator $\underline{E}(20°, 30$ Hz). Thus, if we express Eros' hull estimate in a Cartesian coordinate system

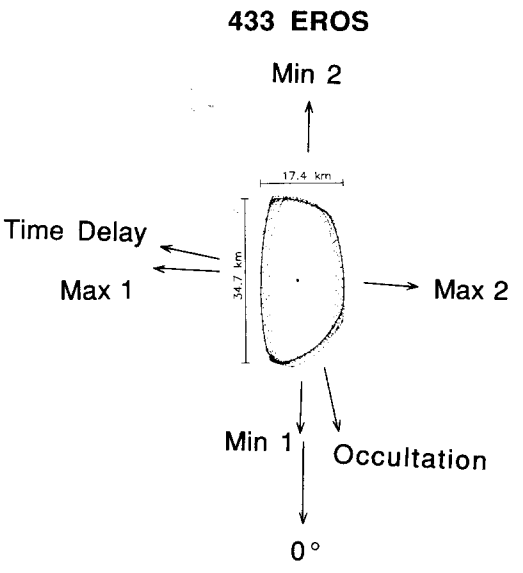

FIG. 6. Bias-corrected estimate of the convex hull of Eros' polar silhouette. Each profile in the central drawing of Fig. 4 has been scaled by the horizontal and vertical correction factors in Table II. The solid profile is our final hull estimate, corresponding to a phase/frequency filter $(\Delta\theta, \Delta f) = (20°, 30\ \text{Hz})$, and the dotted profiles correspond to the other eight choices of $(\Delta\theta, \Delta f)$ in Fig. 4. As discussed in the text, the arrows indicate orientations at epochs of lightcurve extrema (Millis *et al.* 1976), the radar time delay measurement by Campbell *et al.* (1976), and the stellar occultation observations by O'Leary *et al.* (1976).

with x and y axes parallel to the *ellipse's* minor and major axes, respectively, and then multiply the hull's x and y coordinates by 0.82 and 1.00, we can compensate for the most serious bias in our estimator.

We have applied bias corrections to the nine estimates of Eros' hull in Fig. 4. Figure 6 shows a bias-corrected version of the central drawing from Fig. 4, and Table II lists the corresponding hull dimensions. Since we wish to ensure that errors assigned to Eros' hull estimate and derived quantities are not underestimated, we will quote uncertainties based on the *total range* of values spanned by the nine, *bias-corrected* estimations, and whenever practicable will express the results as an interval estimate (Freund and Walpole 1980).

C. Size and Shape of Eros' Polar Silhouette

For the bandwidth equivalents of the maximum and minimum dimensions of Eros' hull, our bias-corrected estimations yield

$$638 \le B_{\max} \le 681\ \text{Hz}$$
$$263 \le B_{\min} \le 329\ \text{Hz}. \qquad (13)$$

Eros' synodic spin period during the radar observations was 0.21954 ± 0.00001 day = 5.2689 ± 0.0002 hr (Dunlap 1976, Table IV). Substituting that value into Eq. (1) yields a conversion factor of (0.05327/cos δ) km Hz^{-1}. Constraints on Eros' pole direction (Dunlap 1976, Millis *et al.* 1976, Scaltriti and Zappalà 1976, Drummond *et al.* 1985, Drummond and Hege 1989) establish

TABLE II

BIAS-CORRECTED EROS HULL ESTIMATES[a]

	Δf = 25 Hz	Δf = 30 Hz	Δf = 35 Hz
	Bias-correction factors from ellipsoid simulations		
	(x, y)	(x, y)	(x, y)
$\Delta\theta$ = 25°	0.84,1.00	0.82,0.98	0.79,0.97
$\Delta\theta$ = 20°	0.86,1.02	0.82,1.00	0.81,0.98
$\Delta\theta$ = 15°	0.89,1.05	0.85,1.01	0.84,0.99
	Maximum dimension (Hz)		
$\Delta\theta$ = 25°	638	650	681
$\Delta\theta$ = 20°	651	651	655
$\Delta\theta$ = 15°	662	653	659
	Minimum dimension (Hz)		
$\Delta\theta$ = 25°	309	326	327
$\Delta\theta$ = 20°	295	326	329
$\Delta\theta$ = 15°	263	303	313
	Elongation		
$\Delta\theta$ = 25°	2.06	1.99	2.08
$\Delta\theta$ = 20°	2.21	2.00	1.99
$\Delta\theta$ = 15°	2.52	2.16	2.11

[a] The three lower 3 × 3 subtables show results of correcting corresponding values in Table I for bias in the hull estimators, by multiplying the maximum and minimum dimensions by the x and y correction factors given in the top subtable.

that $|\delta|$ was no more than $\sim 10°$ from zero during the radar observations, i.e., that cos δ was within a few percent of unity. Thus, converting units establishes a length scale for the extreme dimensions of Eros' hull:

$$34 \leq D_{max} \leq 37 \text{ km}$$
$$14 \leq D_{min} \leq 18 \text{ km}. \quad (14)$$

These intervals are in decent agreement with the extreme dimensions of various axisymmetric models of Eros reported in the literature, including Zellner's (1976) consensus dimensions (16 × 37 km) and Lebofsky and Rieke's (1979) values for a thermal model based on a cylinder with hemispherical ends (16.1 ± 0.8 km × 39.3 ± 2.0 km).

Eros' hull is shaped like a trapezoid whose bases have different lengths and whose sides are distinctly nonparallel. The polar silhouette is clearly not axisymmetric, suggesting that some of the odd-harmonic character of the 1975–1976 optical lightcurves and radar echoes can be attributed to the asteroid's shape, as discussed further below.

D. The Hull's Centroid

In Figs. 4 and 6, the hull's center of rotation, i.e., *Eros'* center of mass, is indicated by a dot, while the *hull's* centroid is marked by a large symbol. The offset of the hull's centroid from Eros' center of mass, between 1 and 2 km, constrains Eros' mass distribution, albeit very loosely. A modest concavity along the silhouette's lower left edge offers a simple explanation for the offset, but there obviously are a myriad of other possibilities.

E. Eros' Echo Power Spectra Revisited

Figure 7 plots weighted sums of the Eros echo spectra within 12 30°-wide windows centered on $\theta = 0°, 30°, \ldots, 330°$. Above each spectrum is a replica of the bias-corrected estimate of Eros' hull (the solid profile in Fig. 6), drawn at the same linear scale as the Doppler axis and at the indicated rotation phase (cf. Fig. 1).

Note how the spectral bandwidth tracks the horizontal breadth of the hull. The reader might wish to follow Eros through a full rotation, exploring the relation between spectral shape and the inclination of the hull's boundary to the line of sight. In contrast to the situation at optical wavelengths, radar backscattering laws for virtually all planetary surfaces studied so far exhibit limb darkening. To the extent that the hull reveals the orientation of surface elements responsible for the radar echoes, we expect some correlation between a spectrum's amplitude at any given Doppler frequency and the angle of incidence at the corresponding point on the hull. *Some* correlation of this sort is indeed present at several phases—more normally oriented portions of the hull often appear to return more echo power.

The 12 spectra comprise six pairs of spectra taken ~180° apart. The differences between "opposing" spectra constitute odd harmonics in Eros' spectral signature, which were noted by Jurgens and Goldstein (1976). These differences, plus the fact that the hull's middle-frequency function $\hat{f}_{mid}(\theta)$ wobbles around zero (Fig. 5), demonstrates that the asymmetry in the shape of Eros' polar silhouette explains that characteristic of the echoes.

F. Rotation Phase of Eros' Hull: Relation to Lightcurve Extrema

A UTC epoch near the middle of the week of Goldstone observations and corresponding to $\theta = 0°$ is 1975 January 23.34758. Millis *et al.* (1976) report epochs of lightcurve extrema, which they identify as Max 1, Min 1, Max 2, and Min 2. Those authors translate epochs to the asteroid's frame, while we retain an observatory-based frame, which is "uncorrected for light time." Taking the difference between these two conventions into account, we find that the Min 1 configuration occurred 0.00063 day, or 54 sec, or 1.0° of rotation phase, before the minimum-breadth configuration.

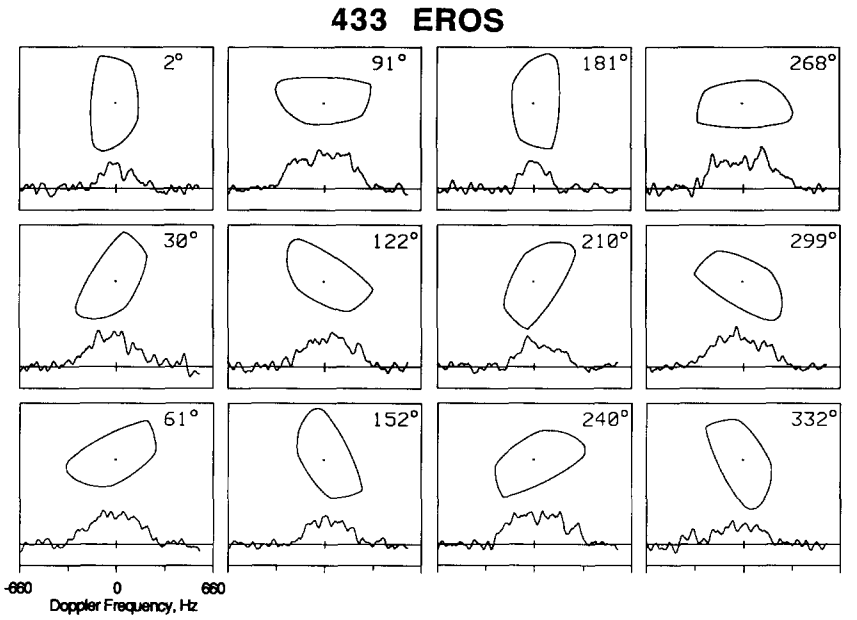

FIG. 7. Eros echo spectra and hull at 12 rotation phases. Weighted sums of spectra within 30°-wide windows have been filtered to a frequency resolution $\Delta f = 40$ Hz and plotted on identical, linear scales of echo power versus Doppler frequency. A horizontal line is drawn at zero echo power. A vertical bar at the origin indicates ± 1 standard deviation of the receiver noise. A replica of Eros hull estimate, the solid profile in Fig. 6, is drawn above each spectrum at the same scale as the Doppler frequency axis and at the indicated, weighted-mean rotational phase. The phases are rarely integral multiples of 30° because the data's phase coverage is not perfectly uniform.

During January 19–26, Max 1 was the primary maximum (~0.1 mag brighter than Max 2), and Min 2 was the primary minimum (~0.1 dimmer than Min 1). Thus, as sketched in Fig. 6, the primary maximum occurred when Eros' longest side was facing Earth. At the secondary maximum, the opposite side of the asteroid faced the viewer and the hull's projected length was the same as at primary maximum, but less of it was normally oriented at secondary maximum than at primary maximum.

If we were dealing with a *two-dimensional* asteroid, then these differences in the distribution of incidence angle, coupled with the assumption that the asteroid is limb-darkened, would furnish a simple explanation for the difference between the lightcurve maxima; the same logic would explain the differences between the lightcurve minima. However, the solar phase angle (i.e., the Sun–Eros–Earth angle) was within 1° of 9° during the radar observations, and very little limb darkening is expected this close to opposition (e.g., French and Veverka 1983, Hapke 1986, Lumme and Bowell 1981).

In the absence of limb darkening (i.e., for purely geometric scattering), odd harmonics in the lightcurve can arise from many different kinds of shape effects and albedo variations. However, the differences between matched extrema constitute roughly 10% of the lightcurve amplitude while optical polarization and color variations are only at the ~1% level (Zellner and Gradie 1976, Larson *et al.* 1976, Pieters *et al.* 1976, Miner and Young 1976, Tedesco 1976, Veeder *et al.* 1976), so it seems likely that the lightcurve

characteristics are caused more by Eros' shape than by photometric heterogeneity.

G. *Lightcurve Inversion: Estimation of Eros' Mean Cross Section*

If Eros' lightcurves are attributable primarily to the asteroid's shape, what can the lightcurves tell us about that shape? Ostro *et al.* (1988b) show that under certain ideal conditions, one can use "convex-profile inversion" of a lightcurve to estimate a profile which, *unlike the hull*, is a two-dimensional *average* of the asteroid's shape. That profile is called the mean cross section, $\underline{C}$, and is defined as the average of the envelopes on all the surface contours parallel to the equator. The ideal conditions for estimating $\underline{C}$ include Condition GEO, that the scattering is uniform and geometric; Condition EVIG, that the viewing-illumination geometry is equatorial; and Condition PHASE, that the solar phase angle ϕ is known and nonzero. The logic behind these conditions is that they collapse the three-dimensional lightcurve inversion problem, which cannot be solved uniquely, into a two-dimensional problem that can.

During late January 1975, the sub-Sun and sub-Earth points were not very far from Eros' equator and, given the 9° solar phase angle, the scattering was probably almost geometric. Condition EVIG, that the sub-Earth and sub-Sun points lie on the equator, and Condition PHASE imply that the solar phase angle's "equatorial component" ϕ_{eq} equals ϕ itself; this component of ϕ creates the mapping between odd harmonics in $\underline{C}$ and those in the lightcurve. If $\phi_{eq} = 0$, then an equatorial lightcurve of a uniform, geometrically scattering asteroid will contain no odd harmonics. For this reason, inversion of an opposition lightcurve furnishes an even-harmonic-only version of $\underline{C}$ called the asteroid's "symmetrized mean cross section," $\underline{C}_s$. The accuracy of an estimate of $\underline{C}$ can be degraded if the value of ϕ used in the inversion is very different from ϕ_{eq}. For Eros, available pole-direction estimates (Dunlap 1976, Millis *et al.* 1976, Scaltriti and Zappalà 1976, Drummond *et al.* 1985, Drummond and Hege 1989) have uncertainties on the order of 15°, so it is hard to say whether ϕ_{eq} is closer to zero or ϕ.

A subtlety of Condition PHASE is that the *sign* of ϕ used in "convex-profile inversion" corresponds to the asteroid's rotation *sense*. The sign is positive if the asteroid rotates through ϕ from the Earth direction to the Sun direction, a configuration that pertains to Eros in late January 1975 if, as deduced by Dunlap (1976) and Morrison (1976), the asteroid's rotation is direct.

Convex-profile inversion of an Eros lightcurve obtained by Tedesco (1976) on Jan 20 at $\phi = 9°$ yields the estimates of $\underline{C}$ and $\underline{C}_s$ shown in Fig. 8. These averages of Eros' shape rotate clockwise and are shown at $\phi = 0°$, as in the hull figures. The Earth direction is toward the bottom of the figure and the Sun direction is 9° clockwise from there.

Our estimate of Eros' mean cross section is "tapered," and some support for the validity of this result is offered by Lebofsky and Rieke (1979), who argue that a tapered shape can help to explain aspects of the asteroid's thermal-infrared signature (i.e., the IR lightcurve as a function of wavelength between 1.2 and 22 μm) observed by those authors and by Morrison (1976). Brown (1985) has used radiometric models based on ellipsoids to demonstrate that diurnal–thermal lightcurves depend dramatically on asteroid shape; however, axisymmetric models might prove inadequate for highly irregular asteroids. In this context, we suggest that our estimate of Eros' mean cross section reveals shape characteristics responsible for odd-harmonic components of the asteroid's thermal-IR "emission" lightcurve as well as phase differences between the emission and "reflected-light" curves.

For the circumstances at hand, we expect the estimate of the mean cross section's breadth ratio, $\beta^* = 2.36$, to be accurate to several percent. We stress that this elongation pertains not to Eros' three-dimensional

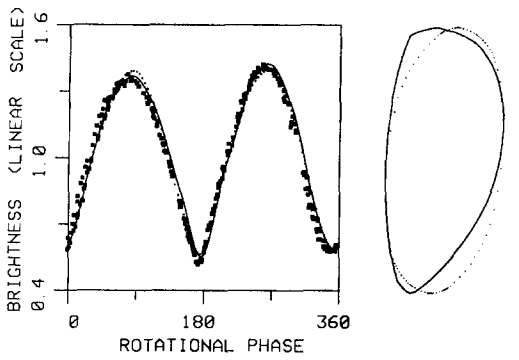

FIG. 8. Eros' mean cross section $\underline{C}$, a two-dimensional *average* of the asteroid's shape. The solid profile is the estimate of $\underline{C}$ and the dotted profile is its symmetrization $\underline{C}_s$, as described in the text. The profiles were derived from Tedesco's (1976) lightcurve via convex-profile inversion (Ostro *et al.* 1988b). The profiles rotate clockwise and are shown at rotational phase $\theta = 0°$. Earth's direction is toward the bottom of the figure and the Sun's direction is 9° clockwise from there. At left, the large symbols are the lightcurve data, the solid curve is a Fourier model fit to the data, and the dotted curve is the model lightcurve corresponding to the estimate of $\underline{C}$.

shape but to a two-dimensional *average* of that shape. Nevertheless, since the "contour averaging" implicit in the definition of $\underline{C}$ and $\underline{C}_s$ is done in radius-of-curvature space (Appendix A of Ostro and Connelly 1984), the largest contours are weighted most heavily, so we should not be surprised that β^* is similar to the hull's elongation, D_{max}/D_{min}, which apparently lies between 1.9 and 2.6 (Table II).

Our estimates of Eros' hull and mean cross section have their longest sides on the receding limb at zero rotational phase. Perhaps that face of Eros lacks prominent positive relief. For the other "sides," we speculate that the apparent differences between the curvatures of $\hat{\underline{C}}$ and $\hat{\underline{H}}$ arise from interesting topographic structure off Eros' equator.

H. Astrometric Results Referenced to Eros' Center of Mass

Echo Doppler frequency. Recall from Section IIIE that one of our goals was to estimate f_0, the Doppler frequency corresponding to echoes from Eros' center of mass, measured with respect to the prediction ephemeris. Figure 4 is the culmination of a search for the value of f_0 that minimizes the postfit RWMS, defined in (10). The optimum estimator gives $f_0 = -17$ Hz and the eight surrounding estimators give values between -24 and -13 Hz. Correcting the observing ephemeris by -17 ± 15 Hz, we obtain the Doppler frequency estimate in Table III.

Echo time delay. During the week of the Goldstone experiment, Eros radar observations were also conducted at Arecibo Observatory, at 70-cm wavelength (Campbell *et al.* 1976). On January 22, a "ranging" waveform was used in attempts to measure the echo's round-trip time delay. The single run yielding detection of an echo was at an epoch (1976 Jan 22, $04^h30^m00^s$ UTC, referred to the instant of reception) close to primary lightcurve maximum (Fig. 6).

Campbell *et al.* report a time delay (150,885,295 ± 5 UTC μsec) measured "to the weighted center of the surface scattering function, which is closer to Earth than, but not precisely located with respect to, the object's center of mass. A best guess of the offset is that it equals the radius of Eros in the line-of-sight at the time of the observation: about 8 km (or 50 μsec in round-trip delay). The quoted error, of course, does not reflect this uncertainty."

Since the subradar latitude was close to zero, it seems reasonable to use our hull estimate to determine that offset. The quoted epoch corresponds to a rotation phase of 258°, at which the hull's center of mass is 9.7 ± 1.5 km (or 65 ± 10 μsec) further from the radar than the subradar point. Adding this offset to the measurement reported by Campbell *et al.* yields an estimate of the time delay corresponding to echoes from Eros' center of mass (Table III).

V. CONCLUSION

Our calculations have elucidated the nonaxisymmetric, quasi-trapezoidal shape of

TABLE III

RADAR ASTROMETRIC RESULTS FOR EROS[a]

Date (1975)	UTC (hh:mm:ss)	Observatory	Transmitter frequency (MHz)	Doppler frequency (Hz)	Time delay (UTC μsec)
Jan 22	04:30:00	Arecibo	430		150,885,360 ± 15
Jan 23	07:00:00	Goldstone	8495	670 ± 15	

[a] Measurements correspond to echoes from the asteroid's center of mass. Epochs are referred to the instant of reception. For the delay entry, our hull estimate has been used to refine a measurement reported by Campbell *et al.* (1976). See text.

Eros' polar silhouette. This result helps to explain the rotation-phase variations in the radar echo spectra and, to a lesser extent, the presence of odd harmonics in the optical lightcurves. Our estimate of Eros' mean cross section C is a "weaker" shape constraint than H; however, visual and thermal-IR lightcurves are *disc-integrated* mappings of precisely those *average* shape characteristics conveyed by the mean cross section.

Unambiguous information about such shape attributes as concavities, nonpolar projections, and nonequatorial curvature components must be sought via stellar-occultation timings, radar delay-Doppler imaging, and speckle interferometry. The sole observations of a stellar occultation by Eros (O'Leary *et al.* 1976) suffer from incomplete ground-track coverage and the lack of photoelectric records. On the other hand, initial efforts to reconstruct images of Eros from speckle interferometric visibility functions are promising (Drummond and Hege 1989). Their speckle image, taken at a solar phase angle ~40° and with the sub-Earth point ~20° from the south pole, has a "peanut-shaped" outline consistent with our hull estimate, and also reveals concavities and brightness variations.

Unlike speckle images and occultation profiles, a radar-derived hull has an a priori orientation with respect to the spin vector; it is conveniently perpendicular, so the spin vector's projection is a point whose location inside the hull can be determined. Consequently, we have been able to tie the 1975 radar time-delay and Doppler-frequency measurements to Eros' center of mass, setting a precedent for small-body radar astrometry. The resultant pair of refined astrometric measurements can be used to improve the accuracy of prediction ephemerides for future ground-based and spacecraft studies of Eros (Yeomans *et al.* 1987).

APPENDIX: PHASE SMOOTHING DETAILS

In the phase-smoothing operation, all the NSPEC spectra whose phases θ_i fall within a specified window are combined into a weighted mean; the weights are $w_i = \gamma_i^{-2}$, where γ_i is the noise level in the i^{th} spectrum (Section II). The noise level γ_w in the weighted-mean spectrum satisfies $\gamma_w^{-2} = \sum \gamma_i^{-2}$.

Let the zero crossings in the weighted-mean spectrum be p_+ and p_-. These two support-function values are associated with rotation phases θ_+ and $\theta_+ + 180°$, and it might seem proper to set θ_+ equal to the weighted mean (θ_w) of the θ_i. However, we wish to ensure that the least-squares Fourier fit (step 2 in Section IIIB) "be aware" of the phases θ_i and noise levels γ_i of the NSPEC parent spectra. Therefore, we let the window's contribution to the support-function "data vector" **p** be *NSPEC identical pairs* of zero crossings (p_+, p_-) whose associated phases (θ_1 and $\theta_1 + 180°$, θ_2 and $\theta_2 + 180°$, . . . , θ_{NSPEC} and $\theta_{\text{NSPEC}} + 180°$) and noise levels are those of the parent spectra. In

different words, we *repeat* the pair (p_+, p_-) NSPEC times in **p**, and the pair's i^{th} appearance is associated with the rotation phase and noise level of the i^{th} parent spectrum.

The error assigned to the i^{th} pair can be written $\varepsilon_i \equiv \Gamma\gamma_i$, where Γ is a proportionality factor whose value is assumed to be constant for the entire Eros data set but is not known a priori. This is all right, because Γ merely scales the data-covariance matrix **M** and drops out of the least-squares calculation of $\hat{\mathbf{x}}$. If the errors $\boldsymbol{\varepsilon}$ are normally distributed and our estimator is unbiased, we would expect the postfit residuals to be χ^2 distributed (Jenkins and Watts 1968, Appendix A4.1). Under this assumption, the value of Γ satisfying

$$(2L - K)\,\Gamma^2 = \sum_{i=1}^{N} [(p_i - \hat{p}_i)/\gamma_i]^2, \quad \text{(A1)}$$

with $K = 2M + 1$ and $2L$ equal to the length of **p**, let us calculate the effective error in the support-function data a posteriori. This procedure was followed in assigning the error bars to the support-function data in Fig. 5.

In exploring phase-averaging approaches, we experimented with independent windows as well as overlapping windows (i.e., running boxes), for a variety of window sizes. The results led us to settle on overlapping windows, offset from each other by multiples of 5°.

ACKNOWLEDGMENTS

We thank P. Ford for a constructive critique of this paper. This research was conducted at the Jet Propulsion Laboratory, California Institute of Technology, under contract with the National Aeronautics and Space Administration.

REFERENCES

BROWN, R. H. 1985. Ellipsoidal geometry in asteroid thermal models: The standard radiometric model. *Icarus* **64,** 53–63.

CAMPBELL, D. B., G. H. PETTENGILL, AND I. I. SHAPIRO 1976. 70-cm radar observations of 433 Eros. *Icarus* **28,** 17–20.

DRUMMOND, J. D., AND E. K. HEGE 1989. Speckle interferometry of asteroids. In *Asteroids II* (R. P. Binzel, T. Gehrels, and M. S. Matthews, Eds.), pp. 171–191. Univ. of Arizona Press, Tucson.

DRUMMOND, J. K., W. J. COCKE, E. K. HEGE, P. A. STRITTMATTER, AND J. V. LAMBERT 1985. Speckle interferometry of asteroids. I. 433 Eros. *Icarus* **61,** 132–151.

DUNLAP, J. L. 1976. Lightcurves and the axis of rotation of asteroid 433 Eros. *Icarus* **28,** 69–78.

FRENCH, L. M., AND J. VEVERKA 1983. Limb darkening of meteorites and asteroids. *Icarus* **54,** 38–47.

FREUND, J. E., AND R. E. WALPOLE 1980. *Mathematical Statistics*, pp. 341–360. Prentice–Hall, Englewood Cliffs, NJ.

HAPKE, B. 1986. Bidirectional reflectance spectroscopy. 4. The extinction coefficient and the opposition effect. *Icarus* **67,** 264–280.

JENKINS, G. M., AND D. G. WATTS 1968. *Spectral Analysis and Its Applications*, pp. 132–139. Holden–Day, San Francisco.

JURGENS, R. F. 1982. Radar backscattering from a rough rotating triaxial ellipsoid with applications to the geodesy of small asteroids. *Icarus* **49,** 97–108.

JURGENS, R. F., AND R. M. GOLDSTEIN 1976. Radar observations at 3.5 and 12.6 cm wavelength of asteroid 433 Eros. *Icarus* **28,** 1–15.

LARSON, H. P., U. FINK, R. P. TREFFERS, AND T. N. GAUTIER III 1976. The infrared spectrum of asteroid 433 Eros. *Icarus* **28,** 95–104.

LEBOFSKY, L. A., AND G. H. RIEKE 1979. Thermal properties of 433 Eros. *Icarus* **40,** 297–308.

LUMME, K., AND E. BOWELL 1981. Radiative transfer in the surfaces of atmosphereless bodies. II. Interpretation of phase curves. *Astrophys. J.* **86,** 1705–1721.

MCGUIRE, J. B., E. R. SPANGLER, AND L. WONG 1961. The size of the solar system. *Sci. Amer.* **204,** 64–72.

MILLIS, R. L., E. BOWELL, AND D. T. THOMPSON 1976. UBV photometry of asteroid 433 Eros. *Icarus* **28,** 53–67.

MINER, E., AND J. YOUNG 1976. Five-color photoelectric photometry of asteroid 433 Eros. *Icarus* **28,** 43–52.

MORRISON, D. 1976. The diameter and thermal inertia of 433 Eros. *Icarus* **28,** 125–132.

O'LEARY, B., B. G. MARSDEN, R. DRAGON, E. HAUSER, M. MCGRATH, P. BACKUS, AND H. ROBKOFF 1976. The occultation of κ Geminorum by Eros. *Icarus* **28,** 133–146.

OSTRO, S. J., AND R. CONNELLY 1984. Convex profiles from asteroid lightcurves. *Icarus* **57,** 443–463.

OSTRO, S. J., R. CONNELLY, AND L. BELKORA 1988a. Asteroid shapes from radar echo spectra: A new theoretical approach. *Icarus* **73,** 15–24.

OSTRO, S. J., R. CONNELLY, AND M. DOROGI 1988b. Convex-profile inversion of asteroid lightcurves: Theory and applications. *Icarus* **75,** 30–63.

PIETERS, C., M. J. GAFFEY, C. R. CHAPMAN, AND

T. B. McCord 1976. Spectrophotometry (0.33 to 1.07 μm) of 433 Eros and compositional implications. *Icarus* **28,** 105–116.

Russell, H. N. 1900. The general perturbations of the major axis of Eros, by the action of Mars. *Astron. J.* **21,** 25–28.

Santaló, L. A. 1976. *Encyclopedia of Mathematics and Its Applications. Integral Geometry and Geometric Probability* (G.-C. Rota, Ed.), Vol. 1, pp. 1–4. Addison–Wesley, Reading, MA.

Scaltriti, F., and V. Zappalà 1976. Photometric lightcurves and pole determination of 433 Eros. *Icarus* **28,** 29–31.

Tedesco, E. F. 1976. UBV lightcurves of asteroid 433 Eros. *Icarus* **28,** 21–28.

Veeder, G. J., D. L. Matson, J. T. Bergstralh, and T. V. Johnson 1976. Photometry of 433 Eros from 0.65 to 2.2 μm. *Icarus* **28,** 79–86.

von Oppolzer, E. 1901. Notiz. Betr. planet (433) Eros. *Astron. Nach.* **154,** 297.

Yeomans, D. K., S. J. Ostro, and P. W. Chodas 1987. Radar astrometry of near-Earth asteroids. *Astron. J.* **94,** 189–200.

Zellner, B. 1976. Physical properties of asteroid 433 Eros. *Icarus* **28,** 149–153.

Zellner, B., and J. Gradie 1976. Polarization of the reflected light of asteroid 433 Eros. *Icarus* **28,** 117–123.